ISSN 1027-5495. Functional Materials, 33, No.3 (2026), p. 562-572
doi:http://dx.doi.org/10.15407/fm33.03.562 © 2026 — SSI "Institute for Single Crystals"
This is an open access article under the CC BY-NC-ND license (http://creativecommons.org/licenses/by-nc-nd/4.0/).

Polarizability of composite nanoparticles with a crescent-shaped metallic shell

R.Yu. Korolkov[1], V.I. Reva[1], R.O. Malysh[1], A.V. Korotun[1,2]

[1] Zaporizhzhia Polytechnic National University, 64 Universytetska Str., Zaporizhzhia, 69011,
[2] G.V. Kurdyumov Institute for Metal Physics of National Academy of Sciences of Ukraine,
36 Academician Vernadsky Blvd., Kyiv, 03142, Ukraine
Corresponding author e-mail: andko@zp.edu.ua

Received January 2, 2026, approved March12, 2026

The problem of determining the optical response of the composite nanoparticles of the "dielectric core – incomplete metallic shell of the variable thickness" type is considered. Relationships for the diagonal components of the polarizability tensor, the absorption and scattering cross-sections, and the radiation efficiency are obtained. The method for calculating the transverse and longitudinal effective relaxation rates is proposed. It is shown that the imaginary parts of the transverse and longitudinal polarizabilities have two maxima each, while the absorption and scattering cross-sections have four maxima each. The classification of the dipole plasmonic modes, which correspond to the maxima of the absorption and scattering cross-sections, is presented. Practical recommendations are provided for the selection of sizes and materials of the particles of the type under the study, which have maximum radiation efficiency in the widest possible spectral range.

Keywords: polarizability tensor, dielectric tensor, shells of variable thickness, surface plasmon resonance, effective relaxation rate.

Поляризовність композитних наночастинок з металевою серпоподібною оболонкою. *Р. Ю. Корольков, В. І. Рева, Р.О. Малиш, А. В. Коротун*

Розглянуто задачу про визначення оптичного відгуку композитних наночастинок типу «діелектричне ядро – неповна металева оболонка змінної товщини». Отримано співвідношення для діагональних компонент тензора поляризовності, перерізів поглинання і розсіювання та радіаційної ефективності. Запропоновано метод обчислення поперечної і поздовжньої ефективних швидкостей релаксації. Показано, що уявні частини поперечної і поздовжньої поляризовностей мають по два максимуми, а перерізи поглинання і розсіювання, відповідно, чотири. Наведено класифікацію дипольних плазмонних мод, які відповідають максимумам перерізів поглинання і розсіювання. Дано практичні рекомендації стосовно підбору розмірів і матеріалів для частинок досліджуваного типу, які мають максимальну радіаційну ефективність в як можна більш широкому спектральному інтервалі

1. Introduction

The localized surface plasmon resonance (SPR) in the noble metallic nanostructures is as a powerful method of the optical control at the nanoscale, which plays the crucial role in the development and improvement of wavelength-tunable (frequency-tunable) optical devices and highly sensitive optical sensors [1–4]. When the incident wave frequency is nearly identical to the collective oscillation frequency of conduction electrons, localized surface plasmons are excited in the metal-

lic nanostructures, causing a strong electromagnetic response and scaling the surface-enhanced Raman scattering (SERS) and surface-enhanced fluorescence (SEF) signals [5, 6]. As is well known, non-destructive and ultra-sensitive spectroscopic methods of SERS and SEF analysis are most suitable for studying the biological objects in the "window of the biological transparency", that is in the visible and near-infrared (NIR) frequency ranges [6]. By controlling the geometric and physical parameters of the nanostructures, such as size and the morphology, it is possible to tune their localized SPR bands over a wide range of the incident radiation [7–10]. Thus, the peaks of the plasmon resonance of the nanostructures can be localized in the "biological transparency window", which increases the spectral figure of merit (FOM) of the biosensors.

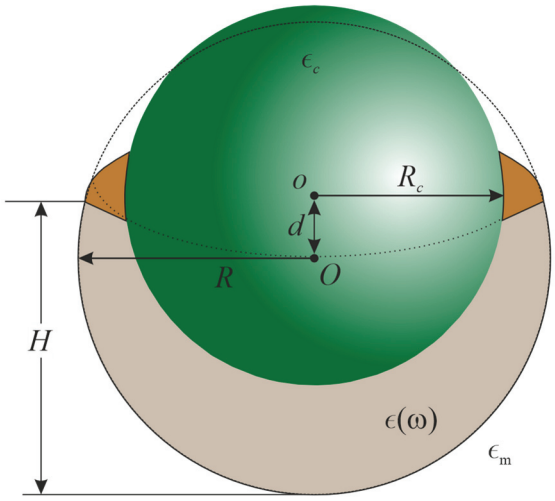

Fig. 1. Crescent-shaped metallic nanostructure

Recently, the considerable efforts have been directed towards the development and the fabrication of various functional plasmonic nanostructures [11, 12]. These nanostructures have maxima in their absorption or extinction spectra. For example, spherical gold or silver nanoparticles have only one extinction peak [13]. Triangular nanoprisms have an intense peak in the absorption spectrum [14]. Nanorods have two plasmonic resonance peaks: the weak transverse mode peak and the intense longitudinal mode peak [15]. Nanoshells also have two plasmon resonance peaks, which are defined as an antibonding mode peak at a higher frequency and a bonding mode peak at a lower frequency, resulting from plasmon hybridization, while the antibonding mode peak is very weak [16]. For nanocubes, several plasmon resonance peaks are observed in the extinction spectra, with only one strong peak being clearly distinguishable [17].

Among the nanostructures synthesized to date, crescent-shaped nanoparticles have attracted considerable attention since their localized surface plasmon resonance peaks are located in the near-infrared range, which leads to increased sensitivity to the properties of the environment [18, 19]. As shown in Fig. 1, the composite nanostructure under the study consists of a dielectric core and an incomplete metallic shell of variable thickness. The resonant plasmonic frequencies of such structures depend on the arc length and the difference between the outer and inner radii [20]. When the size of such a nanostructure becomes less than 25 nm, pure dipole plasmons are excited, and when the size reaches 60 nm and above, the coupling effect becomes more complex, since multipolar plasmon modes are excited [21].

A large number of experimental and theoretical works are devoted to the study of the optical properties of shell nanoparticles [22–27]. The optical properties of spherical particles of the "dielectric core – metallic shell of the constant thickness" type were studied in [25], and particles of the "dielectric core – metallic shell of the variable thickness" type (nanoegg) were studied in [26]. Particles of the "dielectric core – incomplete shell of the constant thickness" type (nanocap) were studied in [27].

From the point of view of application in lateral immunoassay, composite nanoparticles with a crescent-shaped metallic shell are of great interest. To synthesize such nanoparticles, a process of co-assembly of gold nanoparticles coated with oleylamine and aggregated emission luminogens in a polymer matrix is used [28]. This results in the formation of spatially separated fluorescent cores within the polymer matrix and nanoparticles with a crescent-shaped plasmonic shell.

It should be noted that at present, the optical properties of nanoparticles with crescent-shaped shells are studied either using numerical methods [29], or using the transformation plasmonics approach [30, 31]. The disadvantage of the above-mentioned works is that they do not take into account the specific mechanisms of energy loss in crescent-shaped shells, and the transformational plasmonics approach does not allow obtaining the analytical expressions for the components of the polarizability tensor. In this regard, the issues, considered in this work, are relevant.

2. Mathematical model

2.1. Basic relations

We investigate the optical properties of a composite nanostructure consisting of spherical dielectric particles partially covered with a metal shell of variable thickness. The permittivity of the dielectric core is denoted as ϵ_c, and the permittivity of the surrounding medium is denoted as ϵ_m. The geometric parameters of the studied composite nanostructure are shown in Fig. 1.

It should be pointed out that, due to the incompleteness of the shell, the nanoparticle under study loses the spherical symmetry inherent in particles with a complete shell and acquires axial symmetry. In this case, such an optical characteristic of the structure as polarizability is a second-rank diagonal tensor, the components of which are determined by the following expression:

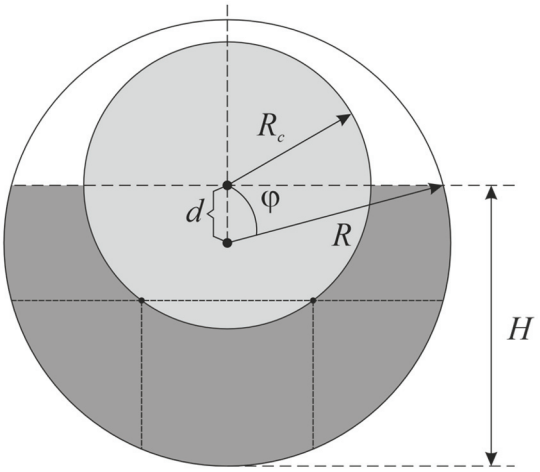

Fig. 2. To the calculation of the volume fraction of the dielectric in the nanoparticle and the relative distance between the centers of the dielectric core and the entire nanoparticle

$$\alpha_{@}^{\perp(\parallel)} = V_0 \frac{\epsilon_{@}^{\perp(\parallel)} - \epsilon_m}{\epsilon_m + \mathcal{L}_{\perp(\parallel)}^{(2)}\left(\epsilon_{@}^{\perp(\parallel)} - \epsilon_m\right)}, \tag{1}$$

where V_0 is the volume of the entire nanoparticle (the total volume of the dielectric core and incomplete metallic shell); $\mathcal{L}_{\perp(\parallel)}^{(i)}$ $(i = 1, 2)$ are the depolarization factors of the dielectric core ($\mathcal{L}_{\perp(\parallel)}^{(1)} = 1/3$) and the entire particle, and the diagonal components of the dielectric tensor of the entire particle

$$\epsilon_{@}^{\perp(\parallel)} = \epsilon_s^{\perp(\parallel)}\left[1 + \tilde{\beta}_c \frac{\epsilon_c - \epsilon_s^{\perp(\parallel)}}{\epsilon_s^{\perp(\parallel)} + \left(\epsilon_c - \epsilon_s^{\perp(\parallel)}\right)\left(\mathcal{L}_{\perp(\parallel)}^{(1)} - \tilde{\beta}_c \mathcal{L}_{\perp(\parallel)}^{(2)}\right)}\right], \tag{2}$$

$\tilde{\beta}_c$ is the bulk content of the dielectric in the nanoparticle; $\epsilon_s^{\perp(\parallel)}$ are the diagonal components of the dielectric tensor of the metallic shell.

The volume of the entire nanoparticle

$$V_0 = V_c + V_s, \tag{3}$$

where the volume of the dielectric core

$$V_c = \frac{4}{3}\pi R_c^3, \tag{4}$$

and the volume of the metallic shell is determined as follows

$$V_s = \int_0^{2\pi} d\varphi \int_0^{\pi-\varphi} \sin\theta d\theta \int_{R_1}^{R_2} r^2 dr. \tag{5}$$

In formula (5), for geometric reasons (Fig. 2)

$$R_1 = \sqrt{R^2 - d^2} - R_c; \quad R_2 = R - R_c + d; \ \operatorname{ctg}\varphi = \frac{d}{R}, \tag{6}$$

therefore, by entering the parameters

$$\beta_c^{1/3} = \frac{R_c}{R}; \ \ \delta_c^{1/3} = \frac{d}{R}, \tag{7}$$

we obtain the final expression for the volume of the shell

$$V_s = \frac{2\pi}{3} R^3 \left[\left(1 - \beta_c^{1/3} + \delta_c^{1/3}\right)^3 - \left(\sqrt{1 - \delta_c^{2/3}} - \beta_c^{1/3}\right)^3\right]\left(1 + \frac{\left(\delta_c/\beta_c\right)^{1/3}}{\sqrt{1 + \left(\delta_c/\beta_c\right)^{2/3}}}\right). \tag{8}$$

Now one can obtain a relation for the volumetric content of the dielectric in the nanoparticle

$$\tilde{\beta}_{\mathrm{c}} = \frac{V_{\mathrm{c}}}{V_{\mathrm{c}} + V_{\mathrm{s}}}. \tag{9}$$

Substituting the expressions (4), (7) and (8) into (9), we finally obtain

$$\tilde{\beta}_{\mathrm{c}} = \left\{1 + \frac{1}{2\beta_{\mathrm{c}}}\left[\left(1 - \beta_{\mathrm{c}}^{1/3} + \delta_{\mathrm{c}}^{1/3}\right)^3 - \left(\sqrt{1 - \delta_{\mathrm{c}}^{2/3}} - \beta_{\mathrm{c}}^{1/3}\right)^3\right]\left(1 + \frac{\left(\delta_{\mathrm{c}}/\beta_{\mathrm{c}}\right)^{1/3}}{\sqrt{1 + \left(\delta_{\mathrm{c}}/\beta_{\mathrm{c}}\right)^{2/3}}}\right)\right\}^{-1}. \tag{10}$$

The depolarization factors, according to the work [32],

$$\mathcal{L}_{\parallel}^{(2)} = \frac{1}{4\pi}\iint\limits_{\Omega}\frac{[\mathbf{r}, d\mathbf{s}]}{r^3},\ \mathcal{L}_{\perp}^{(2)} = \frac{1}{2}\left(1 - \mathcal{L}_{\parallel}^{(2)}\right). \tag{11}$$

Calculating the integral in the first expression in (11), we obtain

$$\begin{aligned}\mathcal{L}_{\parallel}^{(2)} &= \frac{1}{2}\left\{1 + \left(\frac{\delta_{\mathrm{c}}}{\beta_{\mathrm{c}}}\right)^{1/3}\left[1 + \left(\frac{\delta_{\mathrm{c}}}{\beta_{\mathrm{c}}}\right)^{2/3}\right]^{-1/2}\right\},\\ \mathcal{L}_{\perp}^{(2)} &= \frac{1}{4}\left\{1 - \left(\frac{\delta_{\mathrm{c}}}{\beta_{\mathrm{c}}}\right)^{1/3}\left[1 + \left(\frac{\delta_{\mathrm{c}}}{\beta_{\mathrm{c}}}\right)^{2/3}\right]^{-1/2}\right\}.\end{aligned} \tag{12}$$

The diagonal components of the dielectric tensor of the shell material

$$\epsilon_{\mathrm{s}}^{\perp(\parallel)} = \epsilon^{\infty} - \frac{\omega_p^2}{\omega\left(\omega + \mathrm{i}\,\gamma_{\mathrm{eff}}^{\perp(\parallel)}\right)}, \tag{13}$$

where ϵ^{∞} is the contribution of interband electron transitions into the permittivity; ω_p is the plasma frequency; and the effective relaxation rate is determined by the additive contribution of three scattering mechanisms: the bulk relaxation, the surface relaxation and the radiation damping

$$\gamma_{\mathrm{eff}}^{\perp(\parallel)} = \gamma_{\mathrm{bulk}} + \gamma_{\mathrm{s}}^{\perp(\parallel)} + \gamma_{\mathrm{rad}}^{\perp(\parallel)}, \tag{14}$$

The known components of the polarizability tensor can be used to determine such important optical characteristics of the studied nanostructures as the absorption and scattering cross-sections

$$\begin{aligned}C_{@}^{\mathrm{abs}} &= \frac{\omega\sqrt{\epsilon_{\mathrm{m}}}}{c}\,\mathrm{Im}\left(\frac{2}{3}\alpha_{@}^{\perp} + \frac{1}{3}\alpha_{@}^{\parallel}\right);\\ C_{@}^{\mathrm{sca}} &= \frac{\omega^4\epsilon_{\mathrm{m}}^2}{6\pi c^4}\left(\frac{2}{3}\left|\alpha_{@}^{\perp}\right|^2 + \frac{1}{3}\left|\alpha_{@}^{\parallel}\right|^2\right)\end{aligned} \tag{15}$$

and the radiation efficiency

$$\xi_{@}^{\mathrm{rad}} = \left(1 + \frac{C_{@}^{\mathrm{abs}}}{C_{@}^{\mathrm{sca}}}\right)^{-1}. \tag{16}$$

2.2. Effective relaxation rate

Let us now define all the components in the expression (14). The relationships for determining the bulk relaxation rate and the surface relaxation rate have the form [26, 27]

$$\gamma_{\mathrm{bulk}} = \frac{1}{\left\langle\tau_{\mathrm{bulk}}\right\rangle}; \tag{17}$$

$$\gamma_{\mathrm{s}}^{\perp(\parallel)} = \frac{v_{\mathrm{F}}}{\left\langle L_{\mathrm{eff}}^{\perp(\parallel)}\right\rangle}, \tag{18}$$

where $\langle \tau_{\text{bulk}} \rangle$ is the mean time of the bulk relaxation; v_{F} is Fermi electron velocity; $\left\langle L_{\text{eff}}^{\perp(\parallel)} \right\rangle$ are the effective mean lengths of the electron free path in the transverse (longitudinal) directions.

Since the following inequality is true (the case $H = R + d$ is under the study)

$$R < H \le R + R_{\text{c}} + d\,, \tag{19}$$

then

$$\langle \tau_{\text{bulk}} \rangle = \int_0^{\theta^*} \tau_{\text{bulk}} \cos\theta d\theta + \int_{\theta^*}^{\pi-\varphi} 2\tau_{\text{bulk}} \cos\theta d\theta = \tau_{\text{bulk}} \left(2\sin\varphi - \sin\theta^*\right) =$$
$$= \tau_{\text{bulk}} \left\{ 2\left[1 + \left(\frac{\delta_{\text{c}}}{\beta_{\text{c}}}\right)^{2/3}\right]^{-1/2} - \sqrt{1-\beta_{\text{c}}^{2/3}} \right\},$$

where $\tau_{\text{bulk}} = \text{const}$ is the bulk relaxation time, and the bulk relaxation rate

$$\gamma_{\text{bulk}} = \frac{1}{\tau_{\text{bulk}} \left\{ 2\left[1 + \left(\frac{\delta_{\text{c}}}{\beta_{\text{c}}}\right)^{2/3}\right]^{-1/2} - \sqrt{1-\beta_{\text{c}}^{2/3}} \right\}}. \tag{20}$$

The effective mean lengths of the electron free path can be determined as follows

$$\left\langle L_{\text{eff}}^{\perp(\parallel)} \right\rangle = \int_{\Omega} L^{\perp(\parallel)}(\theta) \cos\theta d\theta\,, \tag{21}$$

where Ω is the range of the angles, which correspond to the inequality (19), and $L^{\perp(\parallel)}(\theta)$ are determined by the relationships

$$L^{\perp}(\theta) = \begin{cases} 2R\sin\theta, & 0 < \theta < \theta^*; \\ 2\left(R - R_{\text{c}} + d\cos\theta\right), & \theta^* < \pi - \varphi; \end{cases}$$
$$L^{\parallel}(\theta) = \begin{cases} 2\left(R - R_{\text{c}} + d\cos\theta\right) & 0 < \theta < \theta^*; \\ 2R\cos\theta, & , \ \theta^* < \pi - \varphi. \end{cases} \tag{22}$$

Substituting (22) into (21) and evaluating the integrals, we finally obtain

$$\left\langle L_{\text{eff}}^{\perp} \right\rangle = R\left\{ 1 - \beta_{\text{c}}^{2/3} + 2\left(1 - \beta_{\text{c}}^{1/3}\right)\left[\left[1 + \left(\frac{\delta_{\text{c}}}{\beta_{\text{c}}}\right)^{2/3}\right]^{-1/2} - \sqrt{1-\beta_{\text{c}}^{2/3}}\right] + \right.$$
$$\left. + \delta_{\text{c}}^{1/3}\left[\pi - \arccos\beta_{\text{c}}^{1/3} - \operatorname{arcctg}\left(\frac{\delta_{\text{c}}}{\beta_{\text{c}}}\right)^{1/3} - \beta_{\text{c}}^{1/3}\sqrt{1-\beta_{\text{c}}^{2/3}} - \left(\frac{\delta_{\text{c}}}{\beta_{\text{c}}}\right)^{1/3}\left[1 + \left(\frac{\delta_{\text{c}}}{\beta_{\text{c}}}\right)^{2/3}\right]^{-1}\right]\right\}, \tag{23}$$

$$\left\langle L_{\text{eff}}^{\parallel} \right\rangle = R\left\{ 2\sqrt{1-\beta_{\text{c}}^{2/3}}\left(1 - \beta_{\text{c}}^{1/3}\right) + \delta_{\text{c}}^{1/3}\left(\arccos\beta_{\text{c}}^{1/3} + \beta_{\text{c}}^{1/3}\sqrt{1-\beta_{\text{c}}^{2/3}}\right) + \right.$$
$$\left. + \pi - \arccos\beta_{\text{c}}^{1/3} - \operatorname{arcctg}\left(\frac{\delta_{\text{c}}}{\beta_{\text{c}}}\right)^{1/3} - \beta_{\text{c}}^{1/3}\sqrt{1-\beta_{\text{c}}^{2/3}} - \left(\frac{\delta_{\text{c}}}{\beta_{\text{c}}}\right)^{1/3}\left[1 + \left(\frac{\delta_{\text{c}}}{\beta_{\text{c}}}\right)^{2/3}\right]^{-1}\right\}. \tag{24}$$

The relationships for the transverse and longitudinal components of the radiation attenuation rate, similar to those for metal nanoeggs [26] and nanocaps [27], are of the form

$$\gamma_{\text{rad}}^{\perp(\parallel)} = \frac{2}{9}\frac{V_0}{\epsilon_{\text{m}}^{1/2}}\left(1 - \tilde{\beta}_{\text{c}}\right)\left(\frac{\omega_p}{c}\right)^3 \times \begin{cases} \gamma_{\text{s}}^{\perp(\parallel)}, & \ell_{\text{bulk}}^{s} > 2t_{\text{eff}}; \\ \gamma_{\text{bulk}}, & \ell_{\text{bulk}}^{s} \le 2t_{\text{eff}}, \end{cases} \tag{25}$$

Table 1. Metal parameters (see, for example [26,33] and the references therein)

Metals	Parameters			
	ϵ^{∞}	$v_{\mathrm{F}}, 10^6 \frac{\mathrm{m}}{\mathrm{s}}$	$\hbar\omega_p$, eV	$\hbar\gamma_{\mathrm{bulk}}$, eV
Cu	12.03	1.34	12.6	0.024
Au	9.84	1.41	9.07	0.023
Pt	4.42	2.98	15.2	0.069
Ag	3.70	1.49	9.17	0.016
Pd	2.52	2.84	9.7	0.091

where $\ell^{s}_{\mathrm{bulk}} = v_{\mathrm{F}}\tau_{\mathrm{bulk}}$, and the angular dependence of the shell thickness is determined by the formula

$$t(\theta) = R\left(1 - \beta_{\mathrm{c}}^{1/3} + \delta_{\mathrm{c}}^{1/3}\cos\theta\right). \tag{26}$$

Let us obtain the expression for t_{eff} by the averaging over the angle θ

$$t_{\mathrm{eff}} = \frac{1}{\pi - \varphi}\int_0^{\pi-\varphi} t(\theta)d\theta\,, \tag{27}$$

Substituting $t(\theta)$ from (26) into (27) we obtain

$$t_{\mathrm{eff}} = R\left\{1 - \beta_{\mathrm{c}}^{1/3} + \frac{\delta_{\mathrm{c}}^{1/3}}{\pi - \mathrm{arcctg}\left(\frac{\delta_{\mathrm{c}}}{\beta_{\mathrm{c}}}\right)^{1/3}}\left(1 + \left(\frac{\delta_{\mathrm{c}}}{\beta_{\mathrm{c}}}\right)^{2/3}\right)^{-1/2}\right\}. \tag{28}$$

Formulas (1), (15) and (16), taking into the account the relations (2) – (4), (7), (8), (10), (12) – (14), (18), (20), (23) – (25) and (28) are used to obtain the numerical results.

3. Calculation results and their discussion

The frequency dependencies of the diagonal components of the polarizability tensor, absorption and scattering cross-sections and radiation efficiency were calculated for the nanostructures with different geometric parameters and different core and shell materials. It is assumed that the outer medium is Teflon ($\epsilon_{\mathrm{m}} = 2.3$). The parameters, required for the calculations, are given in Tables 1 and 2, correspondingly.

The frequency dependencies of the real and imaginary parts, as well as the modulus of the diagonal components of the polarizability tensor for $SiO_2@Ag$ nanoparticles in Teflon are presented in Figs. 3 and 4. Similarly to the case of the nanoparticles of the other shape and morphology [27, 34, 35], $\mathrm{Re}\,\alpha_{@}^{\perp(\|)}(\omega)$ are alternating functions of frequency, and $\mathrm{Im}\,\alpha_{@}^{\perp(\|)} > 0$ in the entire spectral range under study. Let us point out that the imaginary parts of the transverse and longitudinal polarizabilities have two maxima each, which correspond to the transverse and longitudinal bond-

Table 2. Dielectric parameters [26]

Value	Core				
	SiO_2	Al_2O_3	Ta_2O_5	Nb_2O_5	TiO_2
ϵ_{c}	2.10	3.10	4.67	6.15	6.50

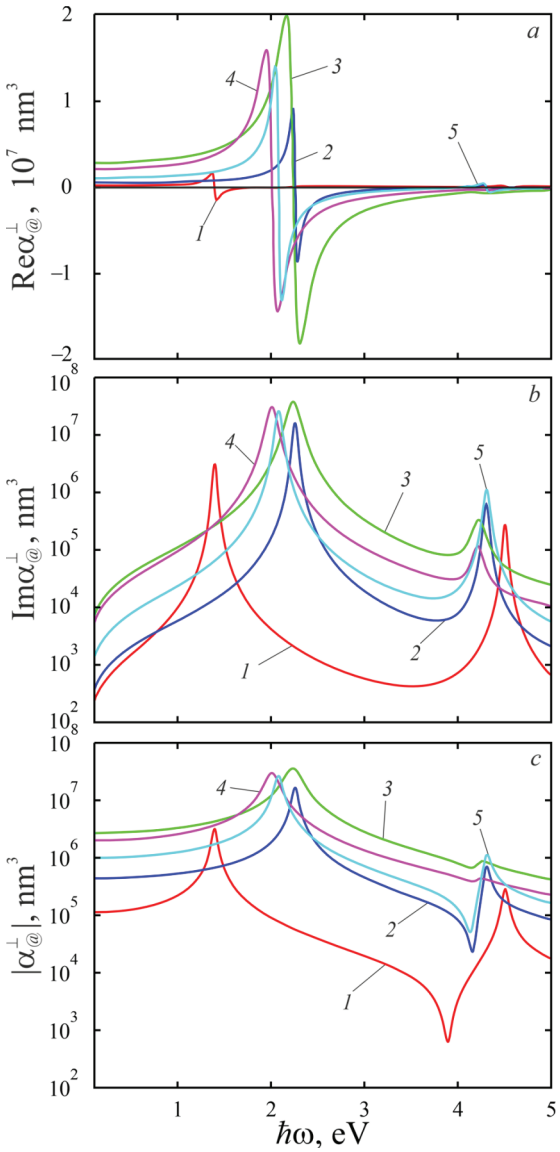

Fig. 3. Frequency dependencies for real (*a*) and imaginary (*b*) parts, as well as for the modulus (*c*) of the transverse component of the polarizability tensor for SiO_2@Ag nanoparticles in Teflon: *1* – $R_c = 15$ nm, $R = 40$ nm, $d = 2$ nm; *2* – $R_c = 15$ nm, $R = 70$ nm, $d = 3$ nm; *3* – $R_c = 15$ nm, $R = 100$ nm, $d = 6$ nm; *4* – $R_c = 10$ nm, $R = 70$ nm, $d = 6$ nm; *5* – $R_c = 20$ nm, $R = 70$ nm, $d = 6$ nm.

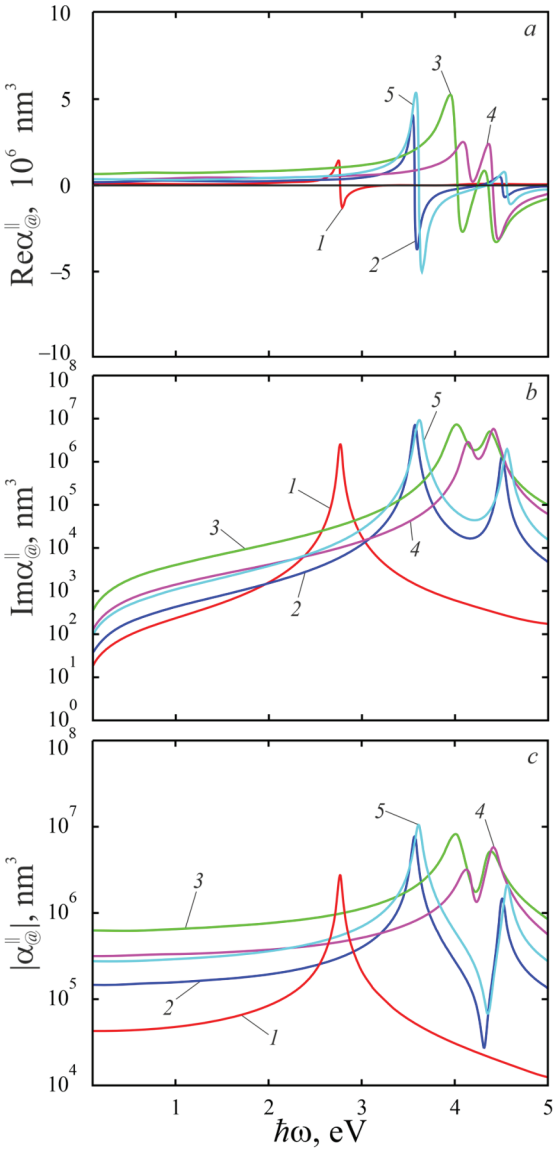

Fig. 4. Frequency dependencies for the real (*a*) and imaginary (*b*) parts, as well as for the modulus (*c*) of the longitudinal component of the polarizability tensor of SiO_2@Ag nanoparticles in Teflon under the same parameters as in Fig. 3

ing and antibonding modes. However, the second maximum of the curve *1* in Fig. 4, *b* is reached at $\hbar\omega > 5$ eV, and therefore is not shown in this figure. According to the ideas of the plasmonic mode hybridization, the bonding modes correspond to lower frequencies. As is known [36], the plasmonic hybridization approach interprets the plasmonic response from the point of view of the interaction of nanostructures of the simplest forms, similar to how the formation of molecular orbitals from atomic orbitals is described in the theory of chemical bonding. In particular, the plasmon resonances of a spherical metallic nanoscale shell are the result of the interaction of plasmons of a metal sphere $|\hbar\omega_s\rangle$ with a dielectric cavity in an infinite metal medium $|\hbar\omega_c\rangle$ (Fig. 5, *a*). The antibonding (loosening) mode with higher frequency (energy) $|\hbar\omega^+\rangle$ and the bonding mode with lower energy $|\hbar\omega^-\rangle$ are two new plasmonic modes. These modes, which are the result of hybridization of plasmons of a metal sphere in a dielectric and a dielectric cavity in a metal, correspond to antisymmetric and symmetric interactions of the modes $|\hbar\omega_s\rangle$ and $|\hbar\omega_c\rangle$. For the metallic crescent-shaped nanostructure investigated in this work, by analogy with

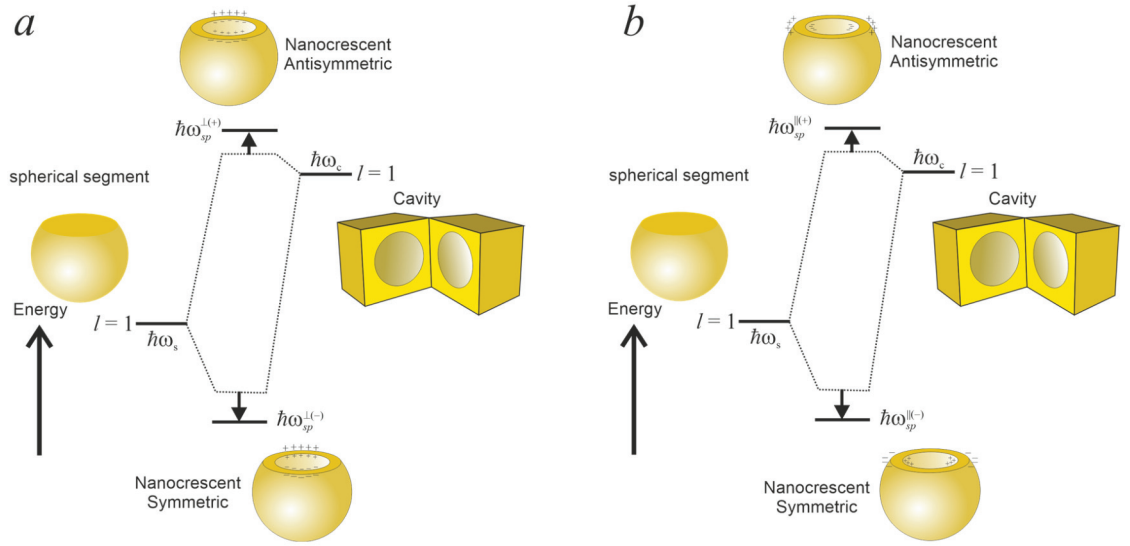

Fig. 5. Schematic energy diagram of the inner Au core and the outer nano-crescent coating depicting plasmonic hybridization: a –transverse mode in the nano-crescent; b –longitudinal mode in the nano-crescent

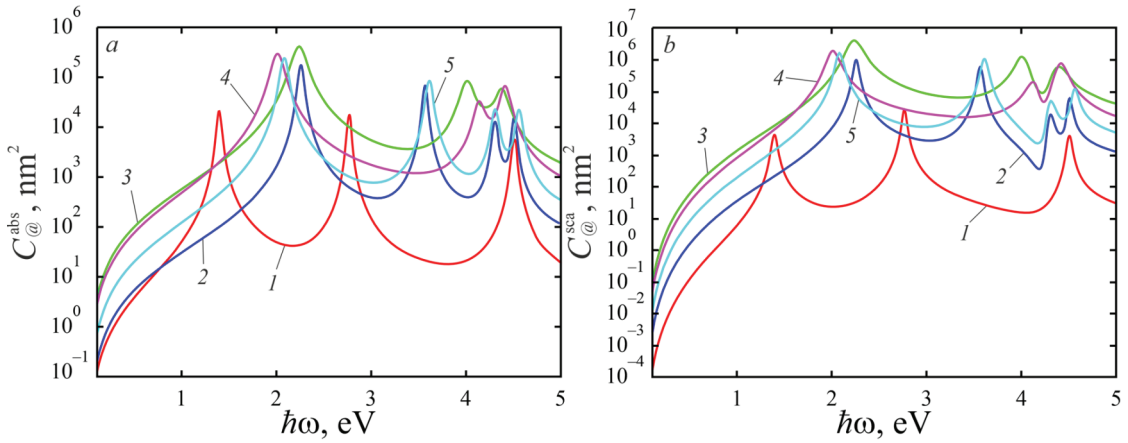

Fig. 6. Frequency dependencies of the absorption cross-section (*a*) and scattering cross-section (*b*) of SiO_2@Ag nanoparticles in Teflon with the same parameters as in Fig. 3

the case of a metallic nanoshell, the simplest forms of plasmonic nanostructures are a spherical dielectric cavity in a metal and a metallic truncated sphere. Transverse and longitudinal resonances in the studied nanostructure should be considered as a result of the interaction of transverse and longitudinal plasmons of a truncated sphere $\left|\hbar\omega_s^{\perp(\parallel)}\right\rangle$ and a plasmon of a spherical dielectric cavity $\left|\hbar\omega_c\right\rangle$ in a metal (Fig. 5, *b*, *c*). It should also noted that the above representations are valid in the case where $\gamma_{\text{eff}}^{\perp(\parallel)} \ll \omega$ and attenuation processes can be neglected.

The results of the calculations indicate that the amplitudes of the maxima corresponding to the bonding transverse mode significantly (by one to two orders of magnitude) exceed the amplitudes of the maxima corresponding to the antibonding transverse mode, while the amplitudes of the maxima corresponding to the longitudinal bonding and antibonding modes are of the same order of magnitude. The spectral positions of the maxima of the antibonding longitudinal and transverse modes are close (they are located in the near ultraviolet frequency range), while the positions of the maxima of the bonding modes are significantly different: while the maxima of the transverse modes are located in the near infrared and red regions, the maxima of the longitudinal modes are located in the blue and near ultraviolet regions. The position of $\max\left\{\text{Im}\,\alpha_{@}^{\perp(\parallel)}\right\}$ also depends on the geometrical parameters of the nanostructure. Thus, the increase in the size of the entire particle at the constant dielectric core radius leads to a "blue" shift of the maxima of the transverse and longitudinal bonding modes and a "red" shift of the maxima of the antibonding modes. In this case, the "blue" shift is more significant than the "red" shift and the splitting of the bonding and antibonding modes in the case of the transverse plasmons is significantly greater.

Frequency dependencies for the absorption and scattering cross-sections for a shell SiO_2@Ag particle are given in Fig. 6. It should be pointed out that the number of maxima of these characteristics and their location correspond to the total contribution of $\mathrm{Im}\,\alpha_{@}^{\perp}$ and $\mathrm{Im}\,\alpha_{@}^{\parallel}$ for the absorption cross-sections and correspond to the contribution of $\left|\alpha_{@}^{\perp}\right|$ and $\left|\alpha_{@}^{\parallel}\right|$ for the scattering cross-sections. It should be noted that the fourth maxima of the curves 1, 3 and 4 in Fig. 6, *a* are achieved at $\hbar\omega > 5$ eV and are therefore not shown in this figure.

Figure 7 shows the frequency dependences of radiation efficiency for SiO_2@Ag nanostructures of different sizes, particles with different dielectric cores and particles with shells made of different metals. Calculations indicate that in the near infrared and visible parts of the spectrum the radiation efficiency is maximum for nanostructures with the maximum volumetric metal content (the curve *3* in Fig. 7, *a*), as well as for particles with a dielectric core with a minimum permittivity (SiO_2). In the case of composite nanoparticles with shells made of different metals and SiO_2 cores, a silver shell should be chosen to achieve maximum radiation efficiency.

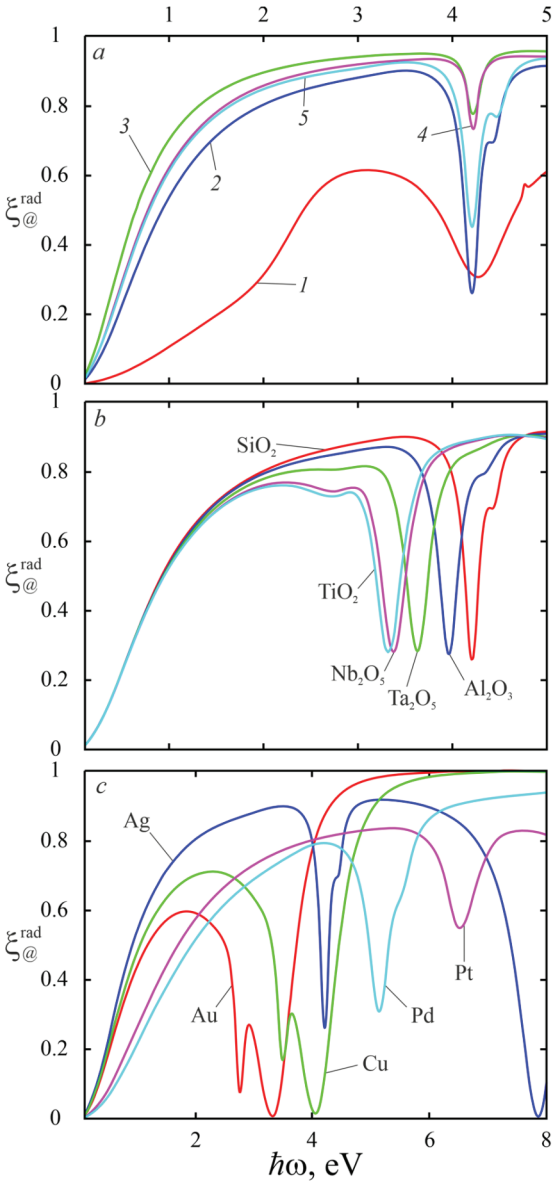

Fig. 7. Frequency dependencies for radiation efficiency of SiO_2@Ag nanoparticles with the same parameters as in Fig. 3 (*a*); nanoparticles D@Ag (*b*), SiO_2@Me (*c*) at $R_c = 15$ nm, $R = 70$ nm, $d = 3$ nm in Teflon

4. Conclusions

Relationships for the frequency dependences of the diagonal components of the polarizability tensor, absorption and scattering cross-sections and radiation efficiency for the metal-dielectric nanostructures of the "dielectric core – metallic crescent-shaped shell" type are obtained. A method has been developed for obtaining the size dependence of the longitudinal and transverse effective relaxation rates.

It is shown that the maxima of the imaginary parts of the transverse and longitudinal components of the polarizability tensor correspond to the bonding (at lower frequency) and antibonding (at higher frequency) modes, and their amplitude and the spectral position are determined by the geometrical dimensions of the nanoparticle and the type of plasmonic modes: an increase in the radius of the entire particle leads to a "blue" shift of the maxima corresponding to the bonding modes and a "red" shift of the maxima corresponding to the antibonding modes. Moreover, although the frequencies of the longitudinal and transverse antibonding modes are close and belong to the near-ultraviolet frequency region, the frequencies of transverse and longitudinal bonding modes differ significantly.

It is demonstrated that the absorption and scattering cross-sections in the entire spectrum have four maxima each, corresponding to the transverse and longitudinal bonding and antibonding resonance modes. This fact is explained by the presence of four maxima of the imaginary parts and modules of the transverse and longitudinal polarizabilities.

It is established that the radiation efficiency in the near-infrared and visible regions of the spectrum is maximum for nanostructures with a higher volumetric metal content, with a dielectric core, the material of which has the lowest permittivity, and the shell material should be a plasmonic metal such as silver.

References

1. B. Luk'yanchuk, N.I. Zheludev, S.A. Maier, N.J. Halas, P. Nordlander, H. Giessen, C.T. Chong, The Fano resonance in plasmonic nanostructures and metamaterials, Nat. Mater. 9 (2010) 707–715. https://doi.org/10.1038/nmat2810.
2. P. Vasa, W. Wang, R. Pomraenke, M. Lammers, M. Maiuri, C. Manzoni, G. Cerullo, C. Lienau, Real-time observation of ultrafast Rabi oscillations between excitons and plasmons in metal nanostructures with J-aggregates, Nat. Photon. 7 (2013) 128–132. https://doi.org/10.1038/nphoton.2012.340.
3. X. Lin, Y. Luo, D. Li, Y. Li, T. Gong, C. Zhao, C. Wang, R. Duan, W. Yue, 2025. Recent advances in localized surface plasmon resonance (LSPR) sensing technologies, Nanotechnology. 36, 202001. https://doi.org/10.1088/1361-6528/adb6a4.
4. J. Zheng, W. Yang, J. Wang, J. Zhu, L. Qian, Z. Yang, An ultranarrow SPR linewidth in the UV region for plasmonic sensing, Nanoscale 11 (2019) 4061–4066. https://doi.org/10.1039/C8NR09703H.
5. P. Offermans, M.C. Schaafsma, S.R. Rodriguez, Y. Zhang, M. Crego-Calama, S.H. Brongersma, J. Gómez Rivas, Universal scaling of the figure of merit of plasmonic sensors, ACS Nano 5 (2011) 5151–5157. https://doi.org/10.1021/nn201227b.
6. S.H. Seo, B.M. Kim, A. Joe, H.W. Han, X. Chen, Z. Cheng, E.S. Jang, NIR-light-induced surface-enhanced Raman scattering for detection and photothermal/photodynamic therapy of cancer cells using methylene blue-embedded gold nanorod@SiO_2 nanocomposites, Biomaterials 35 (2014) 3309–3318. https://doi.org/10.1016/j.biomaterials.2013.12.066.
7. T.K. Sau, A.L. Rogach, F. Jäckel, T.A. Klar, J. Feldmann, Properties and applications of colloidal nonspherical noble metal nanoparticles, Adv. Mater. 22 (2010) 1805–1825. https://doi.org/10.1002/adma.200902557.
8. V. Sharma, Z. Xiao, J. Simmchen, Introduction to Colloidal Particles, in: W. Wang, J. Simmchen, W. Uspal (Eds.), Active Colloids: From Fundamentals to Frontiers, Soft Matter Series, Vol. 20, Royal Society of Chemistry, London, 2024, pp. 1–31. https://doi.org/10.1039/9781837674589-00001.
9. B. Mekuye, R. Höfer, G. Mebratie, 2024. Computational Study of the Effect of the Size-Dependent Dielectric Functions of Gold Nanomaterials on Optical Properties, Advances in Condensed Matter Physics. 2024, 8846112. https://doi.org/10.1155/2024/8846112.
10. N.I. Pavlyshche, A.V. Korotun, V.P. Kurbatsky, R.Yu. Korolkov, Effective polarizability and optical resonances of a square lattice of rod-like metal nanoparticles on a dielectric substrate, Funct. Mater. 32 (2025) 108–114. https://doi.org/10.15407/fm32.01.108.
11. B. Wiley, Y. Sun, Y. Xia, Synthesis of silver nanostructures with controlled shapes and properties, Acc. Chem. Res. 40 (2007) 1067–1076. https://doi.org/10.1021/ar7000974.
12. M. Hu, J. Chen, Z.Y. Li, L. Au, G.V. Hartland, X. Li, M. Marquez, Y. Xia, Gold nanostructures: engineering their plasmonic properties for biomedical applications, Chem. Soc. Rev. 35 (2006) 1084–1094. https://doi.org/10.1039/B517615H.
13. J. Zhu, Y. Wang, L. Huang, Simulation of the medium dielectric constant dependent optical properties for gold nanosphere, Mater. Chem. Phys. 93 (2005) 383–387. https://doi.org/10.1016/j.matchemphys.2005.03.038
14. V.C. Verma, S.K. Singh, R. Solanki, Biofabrication of anisotropic gold nanotriangles using extract of endophytic Aspergillus clavatus as a dual functional reductant and stabilizer, Nanoscale Res. Lett. 6 (2011) 16. https://doi.org/10.1007/s11671-010-9743-6.
15. J.H. Song, F. Kim, D. Kim, P. Yang, Crystal overgrowth on gold nanorods: tuning the shape, facet, aspect ratio, and composition of the nanorods, Chem. Eur. J. 11 (2005) 910–916. https://doi.org/10.1002/chem.200400805.
16. F. Tam, C. Moran, N. Halas, Geometrical parameters controlling sensitivity of nanoshell plasmon resonances to changes in dielectric environment, J. Phys. Chem. B 108 (2004) 17290–17294. https://doi.org/10.1021/jp048499x.
17. J.M. McLellan, Z.Y. Li, A.R. Siekkinen, Y. Xia, The SERS activity of a supported Ag nanocube strongly depends on its orientation relative to laser polarization, Nano Lett. 7 (2007) 1013–1017. https://doi.org/10.1021/nl070157q.
18. Z.A. Lewicka, Y. Li, A. Bohloul, W.W. Yu, V.L. Colvin, 2013. Nanorings and nanocrescents formed via shaped nanosphere lithography: a route toward large areas of infrared metamaterials, Nanotechnology. 24, 115303. https://doi.org/10.1088/0957-4484/24/11/115303.

19. M.-P. Côté, C. Boukouvala, J. Richard-Daniel, E. Ringe, D. Boudreau, A.M. Ritcey, Plasmonic properties of self-assembled gold nanocrescents: implications for chemical sensing, ACS Appl. Nano Mater. 7 (2024) 8783–8791. https://doi.org/10.1021/acsanm.4c00258.
20. Z. Liao, B. Zhou, Y. Huang, S. Li, S. Wang, W. Wen, Fano resonance properties of gold nanocrescent arrays, Appl. Opt. 53 (2014) 6431–6434. https://doi.org/10.1364/AO.53.006431.
21. V. Amendola, R. Pilot, M. Frasconi, O.M. Maragò, M.A. Iatì, 2017. Surface plasmon resonance in gold nanoparticles: a review, J. Phys.: Condens. Matter. 29, 203002. https://doi.org/10.1088/1361-648x/aa60f3.
22. H. Rochholz, N. Bocchio, M. Kreiter, Tuning resonances on crescent-shaped noble-metal nanoparticles, New J. Phys. 9 (2007) 53. https://doi.org/10.1088/1367-2630/9/3/053.
23. J.L. Montaño-Priede, M. Zapata-Herrera, R. Esteban, N. Zabala, J. Aizpurua, An overview on plasmon-enhanced photoluminescence via metallic nanoantennas, Nanophotonics 13 (2024) 4771–4794. https://doi.org/10.1515/nanoph-2024-0463.
24. X. Zhou, K.Y. Liu, N. Zhang, Metal nanostructures with controlled profiles fabricated by nanosphere lithography for localized surface plasmon resonance, in: Plasmons: Theory and Applications, Nova Science Publishers, New York, 2021, pp. 1–41.
25. A.V. Korotun, A.A. Koval', I.N. Titov, Optical absorption of a composite based on bilayer metal–dielectric spherical nanoparticles, J. Appl. Spectrosc. 87 (2020) 240–248. https://doi.org/10.1007/s10812-020-00991-7.
26. R.Yu. Korolkov, R.O. Malysh, V.I. Reva, A.V. Korotun, R.A. Kulykovskyi, 2025. Absorption and scattering of light by metal–dielectric nanoeggs, Condens. Matter Phys. 28, 43702. https://doi.org/10.5488/cmp.28.43702"
27. R.Yu. Korolkov, R.O. Malysh, V.I. Reva, A.V. Korotun, N.V. Shyrokobokova, V.V. Shyrokobokov, 2025. Plasmonic phenomena in metallic nanocap, J. Nano-Electron. Phys. 17, 05022. https://doi.org/10.21272/jnep.17(5).05022.
28. X. Chen, W. Zhan, H. Duan, Y. Su, X. Li, H. Jiang, Y. Xiong, Ben Zhong Tang, X. Huang, 2024. Crescent-shaped Janus nanoassemblies of gold nanoparticles and AIEgens: Enhancing plasmonic and fluorescent activities for colorimetric and ratiometric fluorescence lateral flow immunoassay, Nano Today 58, 102452. https://doi.org/10.1016/j.nantod.2024.102452.
29. Y. Luo, R. Zhao, A.I. Fernandez-Dominguez, Harvesting light with transformation optics, Sci. China Inf. Sci. 56 (2013) 1–13. https://doi.org/10.1007/s11432-013-5031-2.
30. A. Aubry, D.Y. Lei, A.I. Fernández-Domínguez, Y. Sonnefraud, S.A. Maier, J.B. Pendry, Plasmonic light-harvesting devices over the whole visible spectrum, Nano Lett. 10 (2010) 2574–2579. https://doi.org/10.1021/nl101235d.
31. A.I. Fernández-Domínguez, Y. Luo, R. Zhao, J.B. Pendry, Plasmonics and transformation optics, in: World Scientific Handbook of Metamaterials and Plasmonics, World Scientific Series in Nanoscience and Nanotechnology, World Scientific, Singapore, 2017, Chapter 5, pp. 147–196. https://doi.org/10.1142/9789813228726_0005.
32. A.D. Yaghjian, Electric dyadic Green's functions in the source region, Proc. IEEE 68 (1980) 248–263. https://doi.org/10.1109/PROC.1980.11620.
33. A.V. Korotun, H.V. Moroz, R.Yu. Korolkov, Q-factor of plasmonic resonances and field enhancement in the vicinity of spherical metallic nanoparticles, Funct. Mater. 31 (2024) 119–127. https://doi.org/10.15407/fm31.01.119.
34. A.V. Korotun, Quality factor of metal nanoparticles having the shape of a bicone and a bipyramid, in: 2024 IEEE 42nd International Conference on Electronics and Nanotechnology (ELNANO), IEEE, Kyiv, Ukraine, 2024, pp. 185–190. https://doi.org/10.1109/ELNANO63394.2024.10756854.
35. N.I. Pavlyshche, A.V. Korotun, V.P. Kurbatsky, Optical properties of assemblies of disc-shaped metallic nanoparticles, Low Temp. Phys. 51 (2025) 127–132. https://doi.org/10.1063/10.0034657.
36. E. Prodan, C. Radloff, N.J. Halas, P. Nordlander, A hybridization model for the plasmon response of complex nanostructures, Science 302 (2003) 419–422. https://doi.org/10.1126/science.1089171.